

## Article

# Estimating the Risk of Contracting COVID-19 in Different Settings Using a Multiscale Transmission Dynamics Model

Dramane Sam Idris Kanté <sup>1,2</sup> , Aissam Jebrane <sup>2</sup> , Anass Bouchnita <sup>3,\*</sup> and Abdelilah Hakim <sup>1</sup>

<sup>1</sup> LAMAI, Faculty of Sciences and Technics, Department of Mathematics, Cadi Ayyad University, Marrakesh 40140, Morocco

<sup>2</sup> Centrale Casablanca, Complex Systems and Interactions Research Center, Ville Verte, Bouskoura 27182, Morocco

<sup>3</sup> Department of Mathematical Sciences, The University of Texas at El Paso, El Paso, TX 79968, USA

\* Correspondence: abouchnita@utep.edu

**Abstract:** Airborne transmission is the dominant route of coronavirus disease 2019 (COVID-19) transmission. The chances of contracting COVID-19 in a particular situation depend on the local demographic features, the type of inter-individual interactions, and the compliance with mitigation measures. In this work, we develop a multiscale framework to estimate the individual risk of infection with COVID-19 in different activity areas. The framework is parameterized to describe the motion characteristics of pedestrians in workplaces, schools, shopping centers and other public areas, which makes it suitable to study the risk of infection under specific scenarios. First, we show that exposure to individuals with peak viral loads increases the chances of infection by 99%. Our simulations suggest that the risk of contracting COVID-19 is especially high in workplaces and residential areas. Next, we determine the age groups that are most susceptible to infection in each location. Then, we show that if 50% of the population wears face masks, this will reduce the chances of infection by 8%, 32%, or 45%, depending on the type of the used mask. Finally, our simulations suggest that compliance with social distancing reduces the risk of infection by 19%. Our framework provides a tool that assesses the location-specific risk of infection and helps determine the most effective behavioral measures that protect vulnerable individuals.

**Keywords:** COVID-19; airborne transmission; social force models; face masks; physical distancing; hybrid modeling

**MSC:** 70-10; 92-08; 92-10; 92B05; 93A16



**Citation:** Kanté, D.S.I.; Jebrane, A.; Bouchnita, A.; Hakim, A. Estimating the Risk of Contracting COVID-19 in Different Settings Using a Multiscale Transmission Dynamics Model.

*Mathematics* **2023**, *11*, 254. <https://doi.org/10.3390/math11010254>

Academic Editor: Ioannis G. Stratis

Received: 17 October 2022

Revised: 16 December 2022

Accepted: 23 December 2022

Published: 3 January 2023



**Copyright:** © 2023 by the authors. Licensee MDPI, Basel, Switzerland. This article is an open access article distributed under the terms and conditions of the Creative Commons Attribution (CC BY) license (<https://creativecommons.org/licenses/by/4.0/>).

## 1. Introduction

Highly transmissible infectious diseases cause surges of infections and hospitalizations which, overwhelms the healthcare capacity. The risk of getting infected with a particular disease depends on the exposure to infectious individuals, which in turn, depends on the contact patterns between individuals in particular locations [1]. In public areas, pedestrians tend to keep a regular walking velocity and distance from other individuals. It was shown that these motion characteristics vary depending on the location where the individuals move [2]. Understanding the motion properties of pedestrians in different locations would help us gain new insights into the factors that drive the transmission of infectious diseases, such as the coronavirus disease 2019 (COVID-19), in different areas of activity.

Compartmental models are widely used in epidemiology to predict the temporal evolution of epidemics [3–6]. Age-structured compartmental models use contact matrices to calculate the rate of disease transmission. These matrices are usually calculated from surveys where individuals report the average number of individuals with whom they were in contact during a typical day [7–9]. Thus, these surveys rarely consider the temporal changes that shape the patterns of social contacts due to holidays, weekends, non-pharmaceutical

measures or seasonality. Recently, some studies addressed this limitation by studying the effects of seasonality on human-to-human interactions on social contact patterns [10,11]. Still, conventional methods such as surveys do not accurately capture the effect of rush hours and physical distancing on disease propagation [12]. Moreover, collecting surveys requires a lot of time, effort and resources. To overcome these limitations, some researchers resorted to using agent-based models and numerical simulations to create “synthetic populations” whose underlying contact patterns simulate social contact dynamics. For example, a model was constructed to mimic a synthetic Italian society and was used to compute the rates of daily contacts in various locations [13]. Another one used a similar approach to quantify the contact mixing patterns of 26 European countries [14]. Both models study the contact dynamics at the city and country levels but do not investigate mixing patterns in specific places of daily activity.

Social force models are a class of mathematical models that are used to simulate the movement of pedestrians in complex conditions such as crowded areas and panic situations. In these models, Newton’s second law of dynamics is used to compute the movement trajectories of pedestrians [15–17]. An important advantage of these models is that they are physics-based and thus can be analyzed to gain insights into contact patterns in specific locations. Social force models were also previously applied to study the transmission dynamics of infectious diseases. Indeed, a social force model was applied to quantify the impact of non-pharmaceutical interventions on indoor disease transmission [18]. We have previously used a social force model to develop a multi-scale framework that describes COVID-19 transmission dynamics [19–21]. This framework describes transmission through respiratory droplets and contamination by infected surfaces. The characteristic times that describe the evolution of the disease are sampled from the appropriate probabilistic distributions. The model was used to gain insights into the epidemiological characteristics of COVID-19 and the impact of non-pharmaceutical interventions (NPIs). Another important feature of social force models is their ability to describe physical distancing. Indeed, these models assume that individuals tend to keep an interpersonal distance from others. The value of this distance depends on the social and cultural environment as well as the area of activity [2,22]. Social force models are also able to accurately capture the effect of panic on the motion of individuals.

Recent studies have shown that COVID-19 infects mainly through airborne transmission [23–25]. In this route of transmission, infectious individuals produce virus aerosols that diffuse through the air as they talk, cough or sneeze. Large aerosols fall to the ground or contaminate surrounding surfaces while smaller ones keep diffusing in the air for a longer time and can infect susceptible individuals later on. To estimate the risk of infection upon inhaling aerosols, dose-response models were developed to estimate the probability of getting infected upon exposure to viral particles. Wells-Riley models estimate the risk in the case where microbial suspension is well-mixed throughout the room [26–28]. This method was used to evaluate the effectiveness of mitigation measures against tuberculosis [29]. Recently, it was also used to gain insight into COVID-19 transmission [30–32].

In this work, we develop a multi-scale modeling framework to estimate the risk of infection in different locations such as workplaces, schools, shopping centers, residential areas and public spaces. We begin by collecting data on the movement and demographic features in each of these areas. Then, we incorporate these data into our multi-scale framework, which combines a discrete agent-based model with a continuous model for SARS-CoV-2 production, transmission and inhalation. We begin by applying the framework to estimate the risk of infection in different locations. Then, we take advantage of the fidelity of the framework to explore the risk of exposure to individuals with peak viral load. Lastly, we quantify the impact of non-pharmaceutical interventions like face masks and physical distancing and determine their effect on the risk of infection.

## 2. Multiscale Modeling of Disease Transmission

In this section, we introduce a new multi-scale modeling framework that describes COVID-19 transmission and infection. The framework relies on a social force model that captures the movement of individuals in crowded areas. It uses a continuous model to describe the concentration of aerosols in the surrounding environment as well as the accumulation of the virus within individual hosts. The movement model was calibrated using available data on the demographics of pedestrians and their movement features. The chances of contracting the virus are estimated through a probability which depends on the concentration of the inhaled virus.

### 2.1. Social Force Model of Pedestrian Movement

We describe the movement of individuals in specific locations by considering a social force formalism. This framework considers each pedestrian as a particle which is subject to different forces. It uses Newton’s second law of dynamics to calculate the displacement of pedestrians. Social force models were first introduced by Helbing and Molnar [15]. Then, they were used to study pedestrian flows in diverse conditions like bottleneck entrance or panic situations. In our study, we use a previously validated version of social force models that accurately describe the movement of individuals in crowded settings [33,34]. We describe the movement of each individual as in Figure 1:

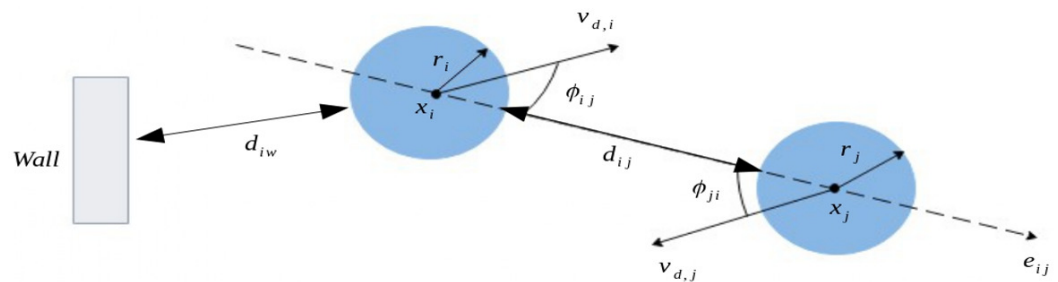


**Figure 1.** Schematic representation of the model parameters defining the interactions between two pedestrians described as blue disks. Each individual has a center  $x_i$  and a radius  $r_i$ . The distancing separating the two individuals  $i$  and  $j$  is described  $d_{ij}$ , while we denote the distance separating an individual from a wall  $w$  by  $d_{iw}$ . The desired velocity of each individual is  $v_{d,i}$  and  $\phi_{ij}$  is the angle between the direction of the desired velocity of  $i$  and the distance between the individual  $i$  and  $j$ .

$$m_i \frac{d\mathbf{v}_i}{dt} = \mathbf{f}_i^{self} + \mathbf{f}_i^{soc} + \mathbf{f}_i^{obs}, \tag{1}$$

where  $m_i$  is the mass of the individual,  $\mathbf{v}_i$  is their velocity,  $\mathbf{f}_i^{self}$  the self-driven force, that describes the adaptation of the pedestrian movement speed to the desired velocity  $v_{d,i}$  given by:

$$\mathbf{f}_i^{self} = m_i \frac{\mathbf{v}_{d,i} - \mathbf{v}_i}{\tau_i}, \tag{2}$$

$$\mathbf{v}_{d,i} = v_{d,i} \mathbf{e}_{d,i}, \tag{3}$$

where  $\mathbf{e}_{d,i}$  is the desired direction,  $\tau_i$  is the relaxation time, which represents the needed time for the pedestrian velocity to adapt to the desired speed (Figure 2). Next, we introduce the social psychological force exerted by pedestrians towards each other. The original form of this force was introduced by Helbing and Molnar [15]. Then, it was modified in recent studies to integrate avoidance between neighboring individuals and allow them to keep the desired distance [33,35]:

$$\mathbf{f}_i^{soc} = \sum \mathbf{f}_{ij}^{soc}, \tag{4}$$

where  $\mathbf{f}_{ij}^{soc}$  is the social psychological force between the  $i$ -th and  $j$ -th individuals, given as follows:

$$\mathbf{f}_{ij}^{soc} = \begin{cases} A_{soc} \exp\left(\frac{d_{ij}-d_{soc}}{\beta_{soc}}\right) \left(\gamma + (1-\gamma)\frac{1+\cos\phi_{ij}}{2}\right) \mathbf{e}_{ij}, & \text{if } d_{ij} < d_{soc} \\ 0, & \text{elsewhere} \end{cases} \quad (5)$$

Here,  $A_{soc}$  represents the magnitude of the social psychological force,  $d_{ij}$  is the distance between the two pedestrians  $i$  and  $j$ ,  $d_{soc}$  is the desired interpersonal distance which describes the distance that individuals tend to keep between them,  $\beta_{soc}$  is the falloff length of the social psychological force,  $\gamma$  describes the effect of interactions taking place behind the individual, taken between 0 and 1 while  $\phi_{ij}$  represents the angle between the desired velocity and the actual one. The interactions of each individual with the environment are captured using the force  $\mathbf{f}_{iw}^{obs}$ , which is an exponential repulsive force that increases when the individual get close to walls:

$$\mathbf{f}_{iw}^{obs} = \begin{cases} A_{obs} \exp\left(\frac{d_{iw}-d_{obs}}{\beta_{obs}}\right), & \text{if } d_{iw} < d_{obs} \\ 0, & \text{elsewhere} \end{cases} \quad (6)$$

Some parameters depend on the age and activity area (Table 1). Their values are provided in Tables S1–S6 of the supplementary material. More details regarding the derivation of the social force model are provided in previous studies [15,16,33,35].

**Table 1.** A summary of the model parameters and their dependency on age and the place of activity. The source of each parameter is also provided.

| Parameter     | Age-Dependent | Activity Area-Dependent | Source                                       |
|---------------|---------------|-------------------------|--|
| $v_{d,i}$     | yes           | yes                     | adapted to the demographic structure [36,37] |
| $\tau_i$      | yes           | no                      | [38,39]                                      |
| $d_{soc}$     | yes           | yes                     | adapted to the demographic structure [22]    |
| $d_{obs}$     | no            | no                      | [35]   |
| $A_{soc}$     | no            | no                      | [33,35,40–43]                                |
| $A_{obs}$     | no            | no                      | [33,35,40–43]                                |
| $\beta_{obs}$ | no            | no                      | [33,35,40–43]                                |
| $\beta_{soc}$ | no            | no                      | [33,35,40–43]                                |
| $\gamma$      | no            | no                      | [33]   |
| $m_i$         | yes           | no                      | Moroccan population weight [44–47]           |

### 2.2. Parameterization of Population Movement Using Real Data

The social force model presents a physical description of the movement of a heterogeneous population of pedestrians. Hence, some parameters can be varied according to age or location to accurately capture the walking pattern of pedestrians. Others will be taken constant for all individuals such as the amplitude and falloff length of the social psychological force ( $A_{soc} = 700$  N;  $A_{obs} = 1000$  N;  $\beta_{soc} = 0.8$  m;  $\beta_{obs} = 0.8$  m) [33,35,40–43].

We stratify the population according to 16 age groups of 5 years, corresponding to age categories ranging from ‘0–5’ to ‘over 75’. We consider that the relaxation time depends on the age according to previous studies [38,39]. The desired interpersonal distances depend on the location and the cultural environment as well as the age of the individuals. Age-specific interpersonal distances are taken according to the values estimated in the literature [2,22]. We consider three types of interpersonal distances: intimate, personal and social distances [22]. The intimate distance corresponds to lengths from 0 to 46 cm,

personal distance represents interactions that keep a length between 46 cm and 122 cm, and social distance refers to lengths from 122 to 210 cm. In our simulations, we consider that individuals maintain intimate distances in residential areas and households, personal distances in schools and workplaces, and social distances in shopping centers and public spaces. Changes in the three distances caused by age are estimated in a previous study [22]. Here, we sample interpersonal distances from a Gaussian distribution fitted to data for each age group (Tables S1–S5 in the Supplementary Material).

We also consider heterogeneity in the desired walking speed that depends on the age of each individual, as well as the location where they walk. For the latter, we consider estimates for walking speeds provided for educational, commercial, mixed, recreational, residential and shopping areas [48] (Tables S1–S5 in the Supplementary Material). In these estimates, residential and shopping areas displayed lower average walking speeds, while educational places had the fastest walking speeds. Another study has shown that walking speed was highest in workplaces and malls [36]. In our work, we use the estimates provided by this study for all locations, except in the residential areas where we use the ones provided by [37].

We sample the ages of the individuals from the Moroccan demographic structure [44–47] (Table S6 in the Supplementary Material). For location-specific simulations, we sample the ages from the distributions corresponding to demographics in the corresponding location [49–53]. We consider the same density for all locations. A summary of collected data is available in the supplemental Material.

### 2.3. Modeling Virus Diffusion and Disease Transmission

#### 2.3.1. Virus Transport and Diffusion

We restrict our study to airborne transmission since it is considered to be the main route of COVID-19 transmission [54–56]. The model accounts for both short-range and long-range airborne transmission as some particles can linger in the air and travel for longer distances while others shortly fall on the floor after their emission [56,57]. Here, we model the transport and diffusion of the virus in the air following a cough or sneeze of an infectious individual. We consider that whenever an individual coughs or sneezes, they produce a concentration of the virus between  $277 \times 10^{-6}$  copies/cm<sup>3</sup> and 36,030 copies/cm<sup>3</sup> [58–60], depending on their viral load, and within a diameter of  $d_0 = 1$  m. Then, the concentration of viral particles is spread to the computational mesh using a radial-basis function [19–21]:

$$W_d(\mathbf{x}) = \begin{cases} \frac{w}{4} \left( 1 + \cos\left(\frac{\pi d(\mathbf{x})}{d_0}\right) \right), & d \leq d_0 \\ 0, & d \geq d_0 \end{cases} \tag{7}$$

where  $d$  is the distance between the position of an infectious coughing person and the surrounding points of the computational grid. We describe the concentration of the virus in the air using the following equation:

$$\frac{\partial C_a}{\partial t}(\mathbf{x}, t) = D\Delta C_a(\mathbf{x}, t) + \alpha W_d(\mathbf{x}) - \mu C_a(\mathbf{x}, t), \tag{8}$$

where  $C_a$  is the concentration of the virus at position  $x$  at time  $t$ ,  $D$  is the virus diffusion rate in the air which varies from 0.2 to 0.8 m<sup>2</sup>/s [57],  $\alpha$  is the percentage of particles that linger in the air following a cough or sneeze, taken equal to 0.585 [61], and  $\mu$  is the rate of virus decay and deposition, considered to be equal to  $\mu = 9.25 \times 10^{-5}$  s<sup>-1</sup> [62]. We apply the Dirichlet boundary conditions  $C_a = 0$  at the walls of the computational domains. Next, we describe the inhaled concentration of SARS-CoV-2 by each susceptible individual:

$$\frac{dC_{acc,i}}{dt} = \rho C_a(\mathbf{x}_i, t) - \gamma C_{acc,i}. \tag{9}$$

Here,  $\mathbf{x}_i$  and  $C_{acc,i}$  describe respectively the position of a susceptible person  $i$  and the accumulated concentration of virus in his respiratory tract,  $\rho = 1.3 \times 10^{-4}$  m<sup>3</sup>/s is the

rate of virus inhalation [63] and  $\gamma = 1.9 \times 10^{-6} \text{ s}^{-1}$  is his virus clearance rate [64], due to humidity or virus-specific antibodies.

We have considered that individuals change the direction of their movement once they reach a boundary and we imposed a Dirichlet condition of  $C_a = 0$  on the four boundaries. This corresponds to the situation where there are impermeable walls surrounding the computational domain.

### 2.3.2. Infection Probability

We use a Well-Riley model to estimate the risk of infection depending on the inhaled concentration of the virus [32]:

$$P_{a,i} = 1 - \exp(-C_{acc,i}I), \tag{10}$$

where  $P_{a,i}$  is the risk of infection of a person  $i$ ,  $C_{acc,i}$  is the concentration of virus that they inhaled and we set  $I = 0.0069 \text{ m}^3/\text{copies}$  [32].

### 2.4. Settings of Numerical Simulations

We consider a computational domain corresponding to a space of  $50 \text{ m} \times 50 \text{ m}$ . At the beginning of each simulation, 100 pedestrians are generated and randomly placed in the domain with an initial velocity set to zero. The initial direction of their movement is chosen to be random. Every 10 s, 30% of pedestrians alter their directions. We also consider that individuals change the direction of their movement when they reach a boundary of the domain. To ensure the robustness of the results and reduce stochastic noises, we assume that infectious individuals have the same demographic and movement characteristics in all simulations. We consider that the ratio of infectious people corresponds to 3% of the population as estimated in Morocco [65,66]. Therefore, three agents are considered to be infectious, and their locations are chosen randomly in each simulation. A snapshot of a numerical simulation is provided in Figure 2. To further calibrate the model, we conduct a sensitivity analysis where we explore the effects of the variable parameters, such as inhalation rate, diffusion coefficient, and movement velocity on the average absorbed virus (Appendix A).

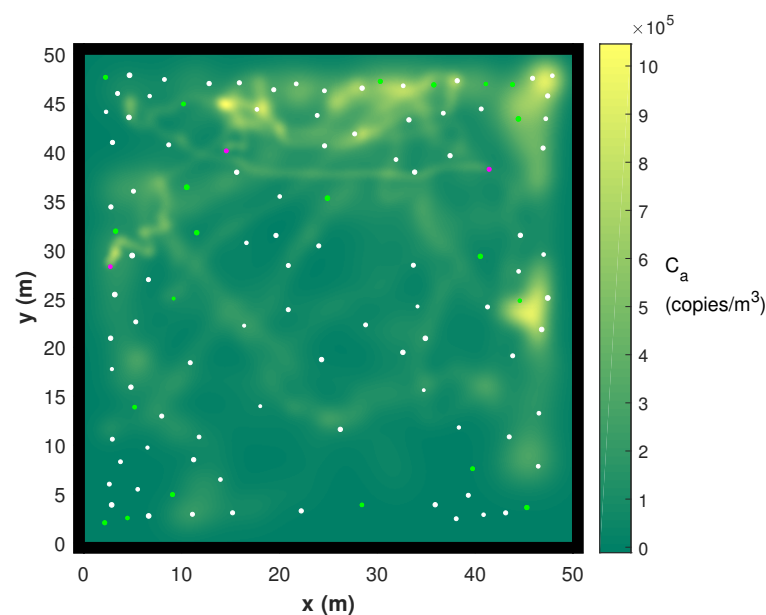


**Figure 2.** A screenshot of a numerical simulation showing the location of pedestrians and the concentration of the virus in the air. White circles describe susceptible individuals. Pink and green ones represent infectious and infected individuals, respectively. The size of each individual correlates with its weight. The green to yellow gradient describes the concentration of the virus in the air.

### 2.5. Computer Implementation

The model was implemented using the software Matlab. The code uses an object-oriented programming paradigm to efficiently couple within- and between-host processes. The CPU time of each simulation corresponding to 10 min of physical time is approximately 2 h on a standard computer with an i5 processor and 16GB RAM.

## 3. Results

### 3.1. Risk of Contracting SARS-CoV-2 Depending on the Age and the Location

#### 3.1.1. Average Infection Risk in Different Areas of Activity

We introduce three infectious individuals that release a viral load  $w = 637,000$  copies/m<sup>3</sup> per second [60]. We run numerical simulations for 10 min; each simulation is repeated multiple times and the median values and 95% confidence intervals are calculated in each case. We set the diffusion coefficient of  $D = 0.05$  m<sup>2</sup>/s, [57]. We estimate the average risk of infection in individuals moving at different places of activity. To achieve this, we calculate the average concentration of inhaled SARS-CoV-2. Figure 3A shows the accumulated inhaled concentration in different locations of activity. Simulations show that individuals moving in residential areas inhale a higher concentration of the virus ( $C_{acc} = 9286 \pm 386$  copies). Individuals moving into workplaces accumulate roughly 21.16% fewer virions than in residential areas ( $C_{acc} = 7281 \pm 110$  copies). While people who move in schools inhale  $C_{acc} = 6573 \pm 190$  copies, which is approximately 8.9% fewer than what individuals inhale when in workplaces. Finally, moving in public spaces and shopping results in inhaling 5.3% fewer virions than in schools. The distribution of the inhaled concentration is represented in Figure 3B. It shows that the concentration follows a Gaussian distribution with a reduced standard deviation for public spaces, shopping centers, schools, and workplaces and a higher standard deviation for residential areas.

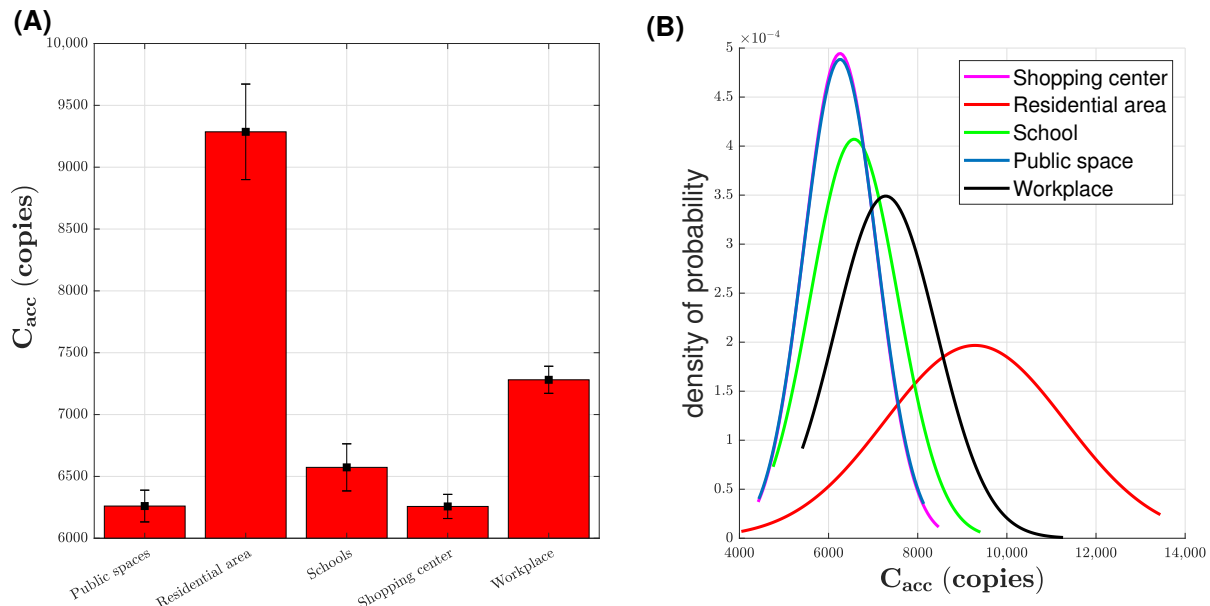


**Figure 3.** The average SARS-CoV-2 inoculum in different activity areas. (A) The mean  $C_{acc}$  in each place of activity, the black ribbons describe the 95% confidence intervals. (B) The distribution of the inhaled virus concentration among individuals in different locations.

Reduced interpersonal distance is generally associated with increased inhalation of the virus. In residential areas, the interpersonal distance is the lowest among all places ( $d_{soc} = 0.46$  m). The effect of the desired velocity depends on the diffusion coefficient, as shown in Appendix A.2. For the considered value, increasing the desired velocity decreases the inhaled concentration. For example, the desired velocity in residential areas, where inhalation is maximal, is equal to  $v_{d,i} = 1.42$  m/s, while it is estimated at  $v_{d,i} = 1.25$  m/s in

schools. Table 2 represents the average and standard deviation of the inhaled concentration in each area as well as the interpersonal distance and the desired velocity.

**Table 2.** The average and standard deviation (SD) inhaled viral charge ( $C_{acc}$ ) in each place of activity. We also provide the social-psychological distance ( $d_{soc}$ ) and the desired walking speed ( $v_{d,i}$ ) in each area.

| Place             | Shopping Center | Residential Area | School | Public Space | Workplace |
|-------------------|-----------------|------------------|--------|--------------|-----------|
| average $C_{acc}$ | 6257            | 9286             | 6573   | 6260         | 7281      |
| SD $C_{acc}$      | 97.6            | 386              | 190    | 128          | 109       |
| $d_{soc}$ (m)     | 2.18            | 0.46             | 1.35   | 2.18         | 1.42      |
| $v_{d,i}$ (m/s)   | 1.37            | 1.42             | 1.25   | 1.28         | 1.40      |

### 3.1.2. Age-Specific Risk of Infection in Each Location

We consider the same simulation settings and we estimate the average inhaled concentration of SARS-CoV-2 for each age group in the five locations. Results in Figure 4A–E show that in shopping centers, the age groups 25–30, 40–45, and 45–50 are more likely to be infected. Results in Figure 4A–E show that in shopping centers, the age groups of 25 to 45 years are more likely to be contaminated. In residential areas, the age groups 15–20, 35–40, and 55–60 are at a higher risk of infection. Simulations of pedestrian movement in schools reveal that the age groups 15–20, 20–25, and 30–35 are more exposed to the infection. While the most susceptible age groups to infection in public spaces are 10–15, 50–55, and 65–70. Finally, the age groups 15–20, 30–35, and 60–65 are at higher risk of infection in workplaces.

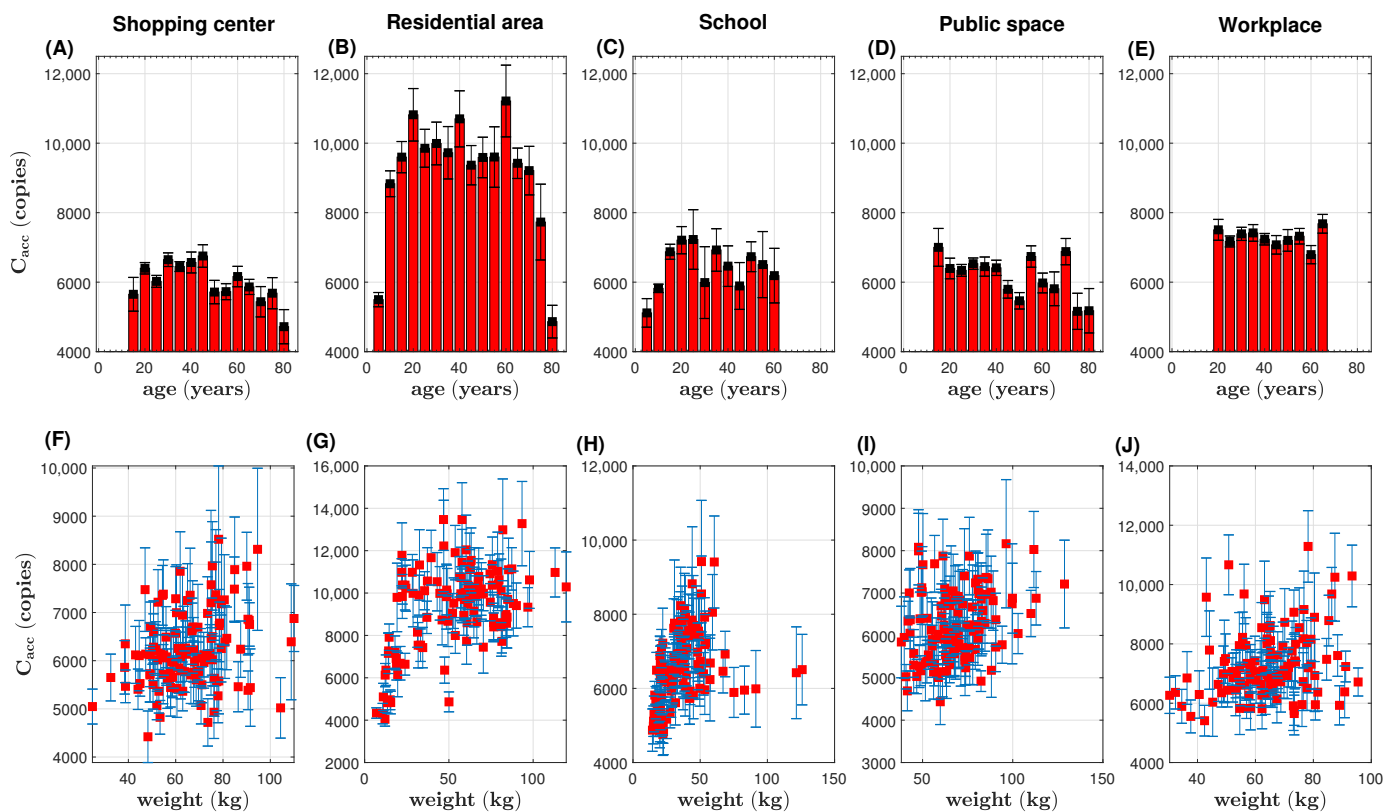


**Figure 4.** Average number of inhaled virus particles per age group in different locations of activity. (A–E) The average inhaled concentration ( $C_{acc}$ ) by age group in shopping centers, residential areas, schools, public spaces, and workplaces. (F–J) Scatterplot of the inhaled concentration  $C_{acc}$  and the weight in shopping centers, residential areas, schools, public spaces and workplaces.

We investigate the association between the weight of individuals and the risk of infection. The data presented in Figure 4F–J show that individuals with increased weight inhale relatively more virions. Although it is difficult to establish a clear relationship between their desired velocity, interpersonal distance and their susceptibility to inhale the virus.

### 3.2. Exposure to Individuals with Peak Viral Load Significantly Upregulates the Risk of Getting Infected

The viral load can be different depending on the course of the infection as well as the vaccination and health status of the infectious individual. Several studies have estimated the viral load at different stages of the infection [58–60]. Collected saliva from COVID-19 patients indicated that the viral load is  $3.3 \times 10^6$  copies/mL [58]. Other studies have reported an average viral load of  $7 \times 10^6$  copies/mL with peak values reaching  $2.39 \times 10^9$  copies/mL [59]. While some experimental works estimated that infectious individuals release a viral concentration that ranges from  $49 \times 10^{-7}$  copies/cm<sup>3</sup> to 0.637 copies/cm<sup>3</sup> [60]. In this section, we estimate the accumulated inhaled concentration ( $C_{acc}$ ) by susceptible individuals under three scenarios: (a) exposure to three infectious individuals with typical viral load who emit a concentration of  $w = 4.9$  copies/m<sup>3</sup> when breathing and  $w = 277,000$  copies/m<sup>3</sup> during coughs. We supposed that these individuals produce two series of coughs after 3 and 6 min of the simulation start. (b) exposure to three infectious individuals who only breathe but emit higher viral concentrations of  $w = 637,000$  copies/m<sup>3</sup>, (c) exposure to three highly infectious individuals with higher viral load who breathe and cough and emit  $w = 637,000$  copies/m<sup>3</sup> during breathing and  $w = 277,000$  copies/m<sup>3</sup> when they cough.

We run numerical simulations using standard parameters that consider the demographic features of the Moroccan population (Table S6 of the Supplementary Material). We consider that all individuals tend to keep an interpersonal distance of 1.22 m and move with a desired velocity equal to 1.34 m/s. Simulations were conducted for 10 min and repeated multiple times to ensure that stochastic noises do not change the outcome and three infectious individuals are chosen randomly in each simulation. Figure 5 shows the average accumulated concentration of the virus under scenarios (a), (b) and (c) in the log scale. These simulations suggest that the viral concentration inhaled is maximal in scenario (c), with individuals inhaling  $C_{acc} = 9.32 \times 10^6 \pm 6.27 \times 10^5$  copies on average. In scenario (b), we estimated that individuals inhale  $C_{acc} = 7308 \pm 174$  copies on average, while the average individual accumulates a concentration of  $C_{acc} = 69 \pm 3.5$  copies in scenario (a).

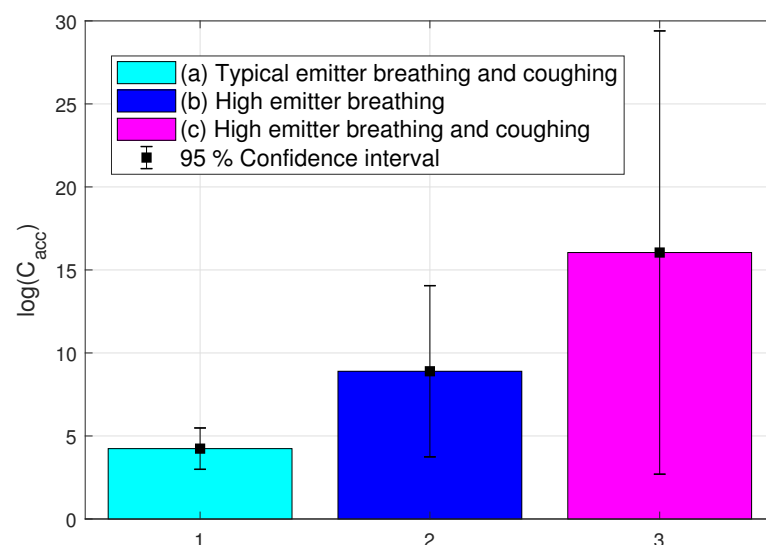


**Figure 5.** The inhaled concentration of SARS-CoV-2 following exposure to three infectious individuals who emit different concentrations of the virus. The risk of infection is estimated in three scenarios

where desired interpersonal distances and desired velocities are homogeneous  $d_{soc} = 1.22$  m,  $v_{d,i} = 1.34$  m/s. The considered scenarios are: (a) typical emitters breathing and making two series of coughs at minutes 3 and 6 of the simulation time. When breathing, they release  $w = 4.9$  copies/m<sup>3</sup> and when they cough they produce the concentration  $w = 277,000$  copies/m<sup>3</sup>, (b) high emitters of SARS-COV-2 who only breathe while moving  $w = 637,000$  copies/m<sup>3</sup>, (c) high emitters breathing and making two series of coughs at different moments. When breathing, they release 637,000 copies/m<sup>3</sup> and when they cough, they emit  $w = 36,030 \times 10^6$  copies/m<sup>3</sup>. The average  $C_{acc}$  is estimated for each scenario. 95% confidence intervals are represented as error bars.

### 3.3. Impact of Non-Pharmaceutical Interventions on the Individual Risk of Infection

#### 3.3.1. Mask Wearing Protects against SARS-CoV-2 Infection Depending on the Compliance Level and the Type of the Used Masks

We investigate the impact of face masking on the risk of infection by considering the effectiveness of three types of face masks in blocking transmission: N95 respirators, surgical masks, and cover clothes. Since not all individuals comply with mask wearing, we assume that only a percentage of these individuals wear masks. In this regard, we run several numerical simulations where the percentage of people wearing masks is varied. Several studies were conducted to estimate the filtering ability of face masks. It was shown the aerosol filtering capacity of face masks is 83–99% for N95 respirators, 42–88% for surgical masks, and 16–23% for cover clothes [67]. In our simulations, we consider the average filtering capacity for each face mask type: 91% for respirators, 65% for surgical masks, and 19.5% for cover clothes. We estimate the reduction of the probability of infection as follows:

$$D_s = 1 - \frac{\text{average } P_{a,i} \text{ when a portion is wearing masks}}{\text{average } P_{a,i} \text{ when no one is wearing masks}} \tag{11}$$

We consider simulations where individuals wear different types of masks and are exposed to three infectious individuals for 10 min. In particular, we study three scenarios where 25%, 50%, and 75% of the population are wearing masks. The results are shown in Table 3. Our simulations were repeated multiple times and the obtained results suggest that when these individuals wear N95 respirators, the reduction in the probability of infection corresponds to  $D_s = 23\%$ , 45%, and 68% when 25%, 50%, and 75% of the individuals wear masks. When individuals wear surgical masks, simulations show a reduction in the probability of infection by 15%, 32% and 49%, when 25%, 50% and 75% of individuals comply to mask wearing mandates. Finally, when individuals wear cover clothes, we estimated that the reduction in infection probability corresponds to 5%, 8% and 13%, when 25%, 50% and 75% of individuals wear masks. The resulting reductions in infection probabilities are compared in Figure 6.

**Table 3.** The average probabilities of infection when different proportions of individuals wear N95 respirators, surgical masks, or cover clothes.

| Percent of Individuals Wearing Mask | N95 | Surgical Mask | Cloth Mask |
|-------------------------------------|-----|---------------|------------|
| 75                                  | 68  | 49            | 13         |
| 50                                  | 45  | 32            | 8          |
| 25                                  | 23  | 15            | 5          |

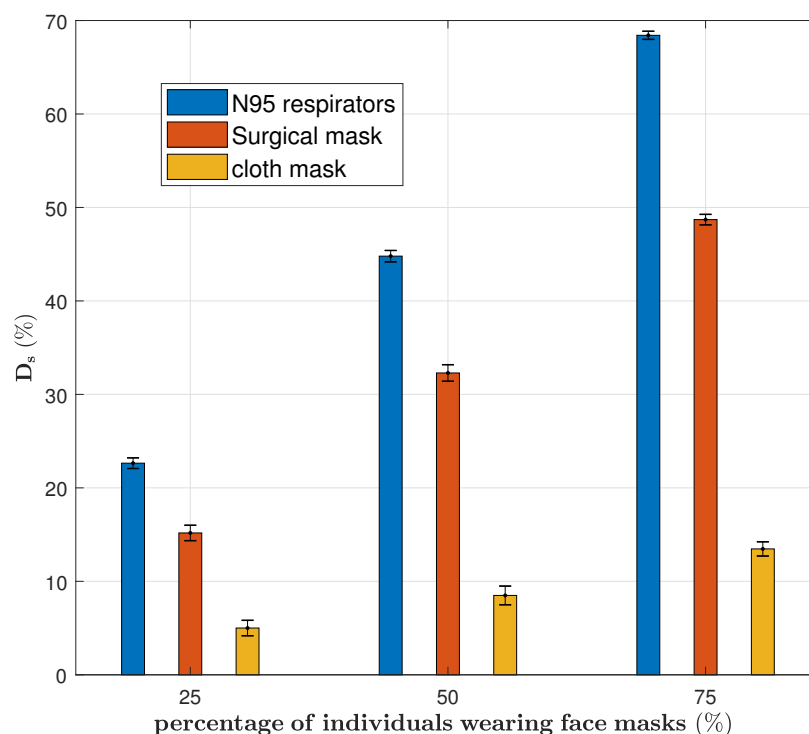


**Figure 6.** The estimated reduction in the average risk of infection as a function of compliance to mask wearing and the type of used masks. The average reduction in the infection probability was estimated for several simulations where proportions of individuals wear masks with different filtering efficacy.

### 3.3.2. Physical Distancing Has Limited Effect on Reducing the Risk of Airborne Transmission

The risk of infection can be minimized if pedestrians keep a certain distance between them. To investigate the impact of physical distancing on the individual risk of infection, we run several numerical simulations where we change the interpersonal distance and estimate the probability of infection. We set the desired movement velocity to 1.34 m/s for all pedestrians in all simulations [15,68,69] and vary the interpersonal distance from 0.5 m to 1.83 m, which corresponds to the recommended distance that individuals should keep [70]. In all simulations, we consider that three infectious individuals are randomly chosen and that they continuously release a typical viral concentration of  $w = 277$  copies/m<sup>3</sup>  $w = 637,000$  copies/m<sup>3</sup>.

As expected, increasing the interpersonal distance decreases the probability of infection (Figure 7). As we increase the interpersonal distance, the probability of infection goes from 0.54 for  $d_{soc} = 0.5$  m to 0.435 for  $d_{soc} = 1.83$  m, while the inhaled virus concentration goes from 7685 copies/m<sup>3</sup> for  $d_{soc} = 0.5$  m to 6065 copies/m<sup>3</sup> for  $d_{soc} = 1.83$  m. This suggests that the physical distancing could reduce the chances of getting infected by only 19%, and the average inhaled concentration by 21%. It is important to note that our work only considers airborne transmission. Other routes of transmission such as direct contact can be significantly stopped by physical distancing.

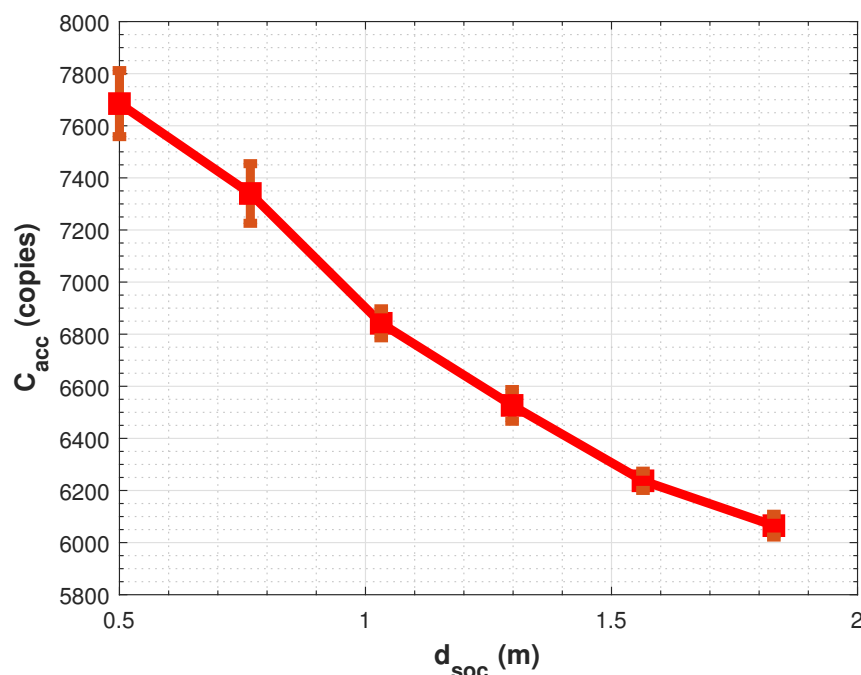


**Figure 7.** Impact of social distancing on the individual chances of infection. The average inhaled concentration of the virus infection as a function of the interpersonal distance ( $d_{soc}$ ). Intervals indicate 95% confidence intervals.

#### 4. Discussion

Airborne transmission is the main route of transmission of COVID-19 [23–25]. It consists of the inhalation of aerosols produced by infectious individuals. The chances of inhaling SARS-CoV-2 particles depend on exposure to infectious individuals as well as the underlying interaction patterns in the area of activity. To model airborne transmission in different social settings, we combine a crowd dynamics framework with a continuous model that describes virus shedding, diffusion and accumulation. The hybrid approach allows the estimation of the chances of both short-range [54–56] and long-range airborne transmission [56,57]. Furthermore, we compute the inhaled concentration of SARS-CoV-2 by each individual to estimate their risk of getting infected. One of the main features of the model is that it incorporates the effect of the mass on the movement of individuals. The mass determines the resistance of individuals to changes in their velocity due to inertia. Further, it regulates the speed by which they adapt their velocity to the desired speed. The model was parameterized using data that reflect social and demographic features of movement in different locations. Then, it was used to gain insights into the age-specific and weight-specific risks of getting infected in several areas of activity. Simulations have shown that residential areas and households represent the area where the risk of infection is high, while shopping centers and public spaces represent locations with reduced infection chances. In general, younger adults were the ones who are at a higher risk of infection in residential areas, schools and shopping centers, while both younger and older adults were at risk in workplaces and public spaces. In residential areas, the age groups 15–20, 35–40, and 55–60 are at a higher risk of infection. Simulations of pedestrian movement in schools reveal that the age groups 15–20, 20–25, and 30–35 are more exposed to the infection. The most susceptible age groups to infection in public spaces, meanwhile, are 10–15, 50–55, and 65–70. The age groups 15–20, 30–35, and 60–65 are at higher risk of infection in workplaces. In the shopping center, the age groups of 25 to 45 years are more likely to be contaminated. These results could be attributed to differences in the relative population, movement speed and preferred interpersonal distance of each age group.

A report has shown most COVID-19 reported cases in Morocco correspond to individuals from 40 to 65, followed by people in the range 25–40 [71]. To compare these results

with our model's predictions, we have merged the results of the five places of activity and illustrated them in Figure 8A, while we have shown data extracted from [71] in Figure 8B. In the report of the Moroccan Ministry of Health from 2020 the age group most likely to be contaminated is 25–40 followed by 40–65, and 15–25, respectively. In our study, the most susceptible age group is 15–25 followed by the age groups 25–40 and 40–65, respectively. This difference could be explained by the assumption that the movement of younger individuals under 40 is characterized by high desired speeds and low desired distances. Both studies suggest that the age group 15–65 is the most susceptible to infection. Furthermore, our simulations suggest that overweight people are at a high risk of getting infected due to a higher exposure period to virus particles. The association between a high body mass index and the risk of contracting COVID-19 was demonstrated in previous works [72,73]. The high exposure period could be explained by their reduced walking speed. The high exposure period could be an explanation for this result.

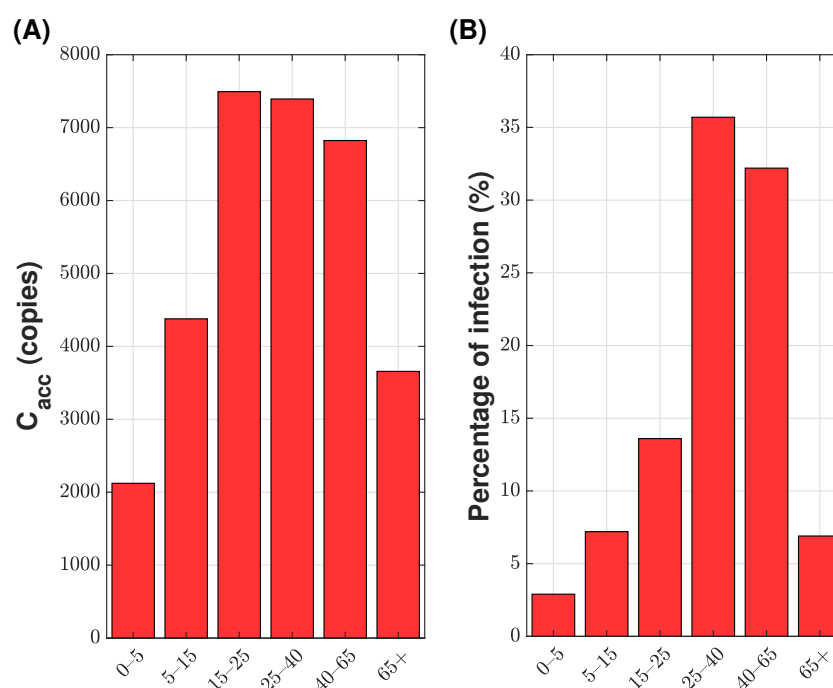


**Figure 8.** Comparison of our age groups that are most likely to be infected with the data reported by the Moroccan Ministry of health on 2020. (A) The estimated average inhaled virus concentration ( $C_{acc}$ ) in all places of activity per age group, calculated using our model. (B) The probability of infection per age group according to the Ministry of health report [71].

Next, we studied the effect of exposure to infectious individuals with peak viral loads. This question was motivated by the heterogeneity in the viral loads of COVID-19 patients, which depends on the progression of the infection as well as the health and vaccination status of the patient. To estimate the individual risk of infection, we run several simulations where a susceptible population is exposed to infectious individuals with normal and peak viral load values. The results show that exposure to individuals with peak viral load increases the average inhaled concentration by over 99%. This agrees with previous studies suggesting that infectious individuals with peak viral loads can be the drivers of superspreading events [74].

Finally, we have studied the impact of mask wearing and physical distancing on the transmission of COVID-19. Using estimates for the filtering capacity of different masks [67,75], we calculated the probability of infections when proportions of the population wear N95 respirators, surgical masks or cloth masks. Our simulations show that the use of N95 respirators, surgical masks, and cloth covers by half of the population decreases the risk of infection by roughly 45%, 32%, and 8%. The impact of physical distancing was also

explored by our model. Numerical simulations suggest that if all individuals comply with physical distancing, this will reduce the probability of getting infected by 19%. These results suggest that physical distancing has a limited impact on stopping airborne transmission. This is probably because of the long-range airborne transmission. As a result, ventilation and face masking should be adopted as the primary measures for stopping COVID-19 airborne transmission indoors [76].

It is important to note that the study relies on a few limitations. First, the model was parameterized to describe the movement of Moroccans in different areas of activity in order to make the conclusions useful for local public health officials. However, we had difficulty finding all data on the movement of the Moroccan population and we had to use values corresponding to other countries in some cases. However, the objective is not to give accurate predictions for the movement patterns in Morocco, but rather to present a framework which can be readily used to estimate the individual risk of infection in different settings. Another limitation concerns uncertainties on the values of some parameters such as the diffusion coefficient of aerosols and the uptake rate. There exist different estimates for these parameters in the literature. To gain insight into the effect of these uncertainties on the findings of our study, we conducted a sensitivity analysis for key parameters. We present the main results of this sensitivity analysis in the Appendix A. Another limitation concerns the considered boundary conditions. While we restricted our study to the situation where individuals are trapped in the computational domain and cannot leave it, it is possible to use the same frameworks to study other situations where there is an inflow and outflow of pedestrians like corridors [77]. The reason behind our choice was to allow the interpretation of the obtained results. Finally, the considered model does not consider the effect of collective motion. It is possible that the movement of some individuals would be affected by the motion of a subgroup of individuals to whom they belong [78]. Incorporating such effects would increase the fidelity of the model. However, it will also make the obtained results harder to interpret. In the future, we will use the same framework to identify the most effective intervention measures for each location and under a wide range of plausible scenarios regarding individuals' motion and infection.

**Supplementary Materials:** The software code is available at <https://www.mdpi.com/article/10.3390/math11010254/s1>.

**Author Contributions:** Conceptualization, A.J. and A.B.; data curation, D.S.I.K.; software, D.S.I.K. and A.J.; formal analysis, A.B. and A.H.; writing—original draft preparation, D.S.I.K.; writing—review and editing, A.B. and A.J.; supervision, A.H. All authors have read and agreed to the published version of the manuscript.

**Funding:** This work is funded by the exceptional research grant for the fight against epidemics and pandemics offered by the Hassan II Academy of Science and Technology, Morocco.

**Data Availability Statement:** The collected data used in this study are available in the supplementary material file.

**Conflicts of Interest:** The authors declare no conflict of interest.

## Appendix A. Sensitivity Analysis

### Appendix A.1. Effects of the Inhalation and Degradation Rates

In this section, we assess the effect of mask wearing on virus exposure and inhalation. We consider that each individual moves with a velocity equal to 1.34 m/s [15,68,69] and tends to keep a personal distance of 1.22 m from other individuals [2]. Other parameters related to the distribution of the mass and relaxation time are available in Table S6 of the supplementary material. In the simulations, we consider that individuals who do not wear face masks inhale the virus and eliminate it at the same rates, regardless of their age or weight. We set the viral load of all infectious individuals to  $w = 1248$  copies/cm<sup>3</sup>.

To estimate the effect of mask wearing, we run several numerical simulations where we compute the effect of the virus inhalation and elimination rates during five minutes

(Figure A1). As expected, increasing the inhalation rate significantly increases the average absorbed virus, while upregulating the elimination rate reduces it. In particular, simulations show increasing the elimination rate delayed the onset of the accumulation of the virus.

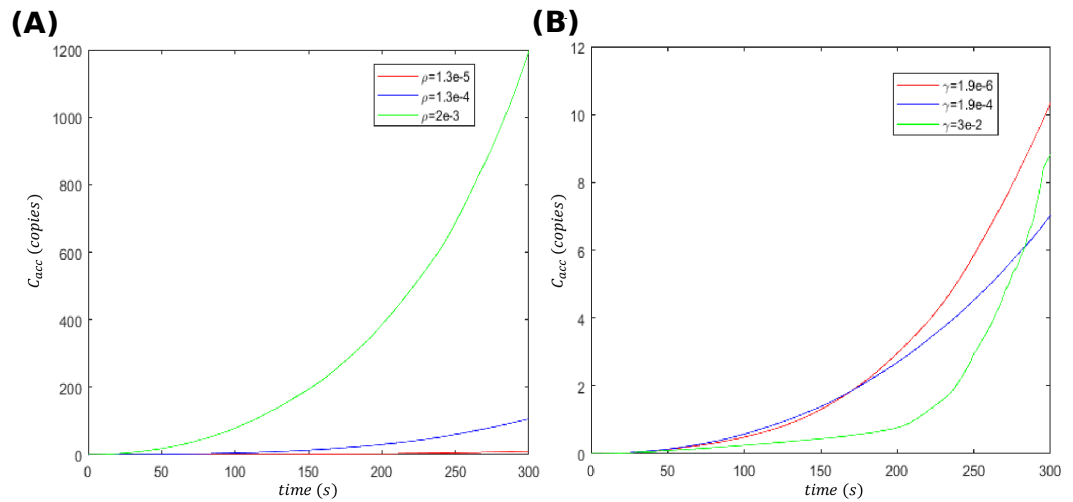


**Figure A1.** The impact of the virus inhalation and virus clearance rates. (A) The average  $C_{acc}$  for three values of the inhalation rate  $\rho = 1.3 \times 10^{-5}$ ,  $1.3 \times 10^{-4}$ ,  $2 \times 10^{-3}$  m<sup>3</sup>/s. (B) The average  $C_{acc}$  for three values of the virus clearance rate  $\gamma = 1.9 \times 10^{-6}$ ,  $1.9 \times 10^{-4}$ ,  $3 \times 10^{-2}$  s<sup>-1</sup>.

*Appendix A.2. Impact of the Coefficient of Diffusion, Velocity and Interpersonal Distances on the Risk of Infection*

We investigate the impact of the diffusion coefficient  $D$  of virus particles in the air on the risk of infection. Three infectious persons are randomly chosen among the populations with a viral load equal to  $w = 277$  copies/cm<sup>3</sup>. We consider that all individuals move with a velocity 1.34 m/s [15,68,69] and tend to maintain a personal distance of 1.22 m [2]. Other parameters such as the weight and the relaxation time are provided in Table S6 of the supplementary material. Results shown in Figure A2 suggest that higher diffusion of viral particles leads to decreased concentration of the absorbed virus on average. High values of the diffusion coefficient imply frequent long-range airborne transmission [57]. This constitutes a threat for long exposure time in the presence of a COVID-19 high emitter who emits 36,030 copies/cm<sup>3</sup> during a cough [60].

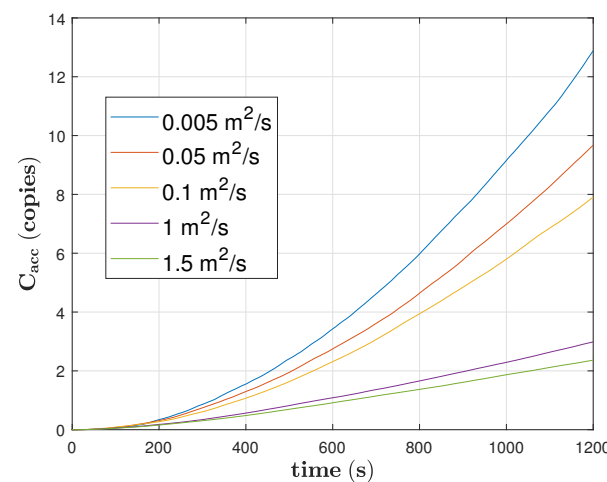


**Figure A2.** The impact of diffusion coefficient on the accumulation of the virus. Other parameters are fixed and the considered population is homogeneous.

### Appendix A.3. Impact of the Walking Velocity on Virus Contraction

We continue our investigation by assessing the impact of the velocity. We set the desired distance for all individuals to 1.22 m [2] and vary the velocity from 0.5 m/s to 1.66 m/s. Results show the diffusion coefficient modulates the relationship between velocity and risk of infection: for high diffusion coefficient values, individuals who walk fast do not accumulate a high concentration of the virus (Figure A3A). As discussed in the previous section when  $D$  is high, particles travel long distances ( $>3$  m) so this results in a reduction of the exposure time to the virus when a susceptible person moves faster. For low values of  $D$  an increase in the velocity increases  $C_{acc}$  in Figure A3B. Indeed, the number of contacts raises when the velocity increases. This situation is similar to rush hours in metro stations. A previous study raises the uncertainty about atmospheric diffusivity so the value of  $D$  presents some variability [57]. In another study [79], it was reported that the diffusion coefficient depends on environmental conditions.

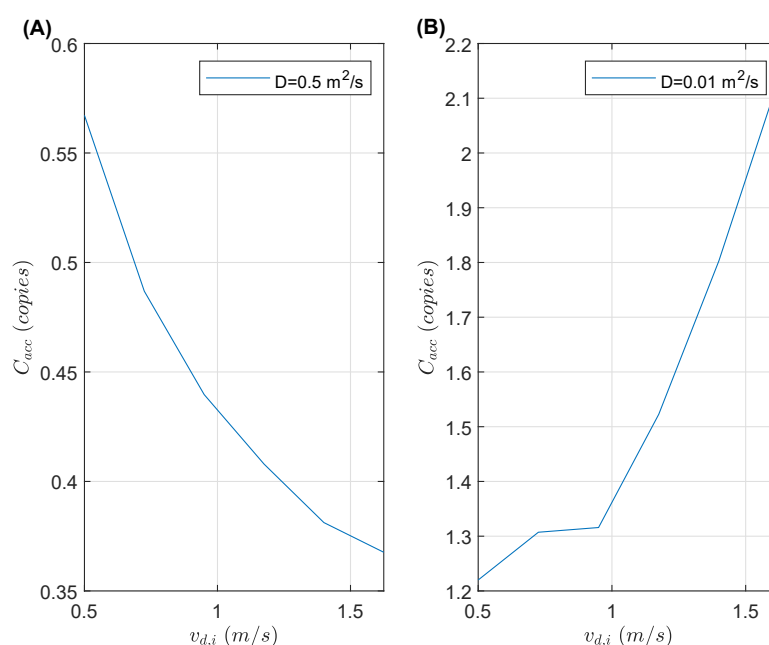


**Figure A3.** Impact of the walking velocity on the risk of infection in a homogeneous population  $d_{soc} = 1.22$  m; with three infectious persons who continuously release a viral load  $w = 277$  copies/m<sup>3</sup>. The coefficient of diffusion moderates the relationship between velocity and risk of infection. We represent the impact of the velocity on  $C_{acc}$  for a diffusion coefficient  $D = 0.5 \text{ m}^2/\text{s}$  (A), and the impact of the velocity on  $C_{acc}$  for  $D = 0.01 \text{ m}^2/\text{s}$  (B).

## References

1. Feehan, D.; Mahmud, A. Quantifying population contact patterns in the United States during the COVID-19 pandemic. *Nat. Commun.* **2021**, *12*, 893. [[CrossRef](#)]
2. Hall, E.T. *The Hidden Dimension*; Doubleday: Garden City, NY, USA; New York, NY, USA, 1966.
3. Kermack, W.O.; McKendrick, A.G.; Walker, G.T. A contribution to the mathematical theory of epidemics. *Proc. R. Soc. Lond. A* **1927**, *115*, 700–721. [[CrossRef](#)]
4. Hethcote, H.W. Three Basic Epidemiological Models. In *Applied Mathematical Ecology*; Levin, S., Hallam, T., Gross, L., Eds.; Springer: Berlin/Heidelberg, Germany; New York, NY, USA, 1989; pp. 119–144.
5. Carsten, K.; Tariq, H.; Maya, G.; Nils, T.; Kaare, G. Methods for estimating disease transmission rates: Evaluating the precision of Poisson regression and two novel methods. *Sci. Rep.* **2017**, *7*, 9496. [[CrossRef](#)]
6. Ghosh, S.; Volpert, V.; Banerjee, M. An epidemic model with time-distributed recovery and death rates. *Bull. Math. Biol.* **2022**, *84*, 78. [[CrossRef](#)]
7. Mossong, J.; Hens, N.; Jit, M.; Beutels, P.; Auranen, K.; Mikolajczyk, R.; Massari, M.; Salmaso, S.; Tomba, G.S.; Wallinga, J.; et al. Social Contacts and Mixing Patterns Relevant to the Spread of Infectious Diseases. *PLoS Med.* **2008**, *5*, e74. [[CrossRef](#)] [[PubMed](#)]

8. Prem, K.; Zandvoort, K.V.; Klepac, P.; Eggo, R.M.; Davies, N.G.; Center for the Mathematical Modelling of Infectious Diseases COVID-19 Working Group; Cook, A.R.; Jit, M. Projecting contact matrices in 177 geographical regions: An update and comparison with empirical data for the COVID-19 era. *PLoS Comput. Biol.* **2021**, *17*, e1009098. [[CrossRef](#)]
9. Prem, K.; Cook, A.R.; Jit, M. Projecting social contact matrices in 152 countries using contact surveys and demographic data. *PLoS Comput. Biol.* **2017**, *13*, e1005697. [[CrossRef](#)] [[PubMed](#)]
10. Huang, Y.; Cai, X.; Zhang, B.; Zhu, G.; Liu, T.; Guo, P.; Xiao, J.; Li, X.; Zeng, W.; Hu, J.; et al. Spatiotemporal heterogeneity of social contact patterns related to infectious diseases in the Guangdong Province, China. *Sci. Rep.* **2020**, *10*, 6119. [[CrossRef](#)] [[PubMed](#)]
11. Dorélien, A.; Ramen, A.; Swanson, I.; Hill, R. Analyzing the demographic, spatial, and temporal factors influencing social contact patterns in U.S. and implications for infectious disease spread. *BMC Infect. Dis.* **2019**, *21*, 1009. [[CrossRef](#)]
12. Eames, K.T.D.; Tilston, N.L.; Brooks-Pollock, E.; Edmunds, W.J. Measured Dynamic Social Contact Patterns Explain the Spread of H1N1v Influenza. *PLoS Comput. Biol.* **2012**, *8*, e1002425. [[CrossRef](#)]
13. Iozzi, F.; Trusiano, F.; Chinazzi, M.; Billari, F.C.; Zagheni, E.; Merler, S.; Ajelli, M.; Del Fava, E.; Manfredi, P. Little Italy: An Agent-Based Approach to the Estimation of Contact Patterns—Fitting Predicted Matrices to Serological Data. *PLoS Comput. Biol.* **2010**, *6*, e1001021. [[CrossRef](#)] [[PubMed](#)]
14. Fumanelli, L.; Ajelli, M.; Manfredi, P.; Vespignani, A.; Merler, S. Inferring the Structure of Social Contacts from Demographic Data in the Analysis of Infectious Diseases Spread. *PLoS Comput. Biol.* **2012**, *8*, e1002673. [[CrossRef](#)] [[PubMed](#)]
15. Helbing, D.; Molnár, P. Social force model for pedestrian dynamics. *Ann. Solid Struct. Mech.* **1995**, *51*, 4282–4286. [[CrossRef](#)] [[PubMed](#)]
16. Helbing, D.; Farkas, I.; Vicsek, T. Simulating dynamical features of escape panic. *Nature* **2000**, *407*, 487–490. [[CrossRef](#)] [[PubMed](#)]
17. Helbing, D.; Farkas, I.; Molnar, P.; Vicsek, T. Simulation of pedestrian crowds in normal and evacuation situations. In *Pedestrian and Evacuation Dynamics*; Schreckenberg, M., Sharma, S.D., Eds.; Springer: Berlin, Germany, 2002; pp. 21–58.
18. Xiao, Y.; Yang, M.; Zhu, Z.; Yang, H.; Zhang, L.; Ghader, S. Modeling indoor-level non-pharmaceutical interventions during the COVID-19 pandemic: A pedestrian dynamics-based microscopic simulation approach. *Transp. Policy* **2021**, *109*, 12–23. [[CrossRef](#)]
19. Bouchnita, A.; Jebrane, A. A hybrid multi-scale model of COVID-19 transmission dynamics to assess the potential of non-pharmaceutical interventions. *Chaos Solitons Fractals* **2020**, *138*, 109941. [[CrossRef](#)]
20. Bouchnita, A.; Jebrane, A. A multi-scale model quantifies the impact of limited movement of the population and mandatory wearing of face masks in containing the COVID-19 epidemic in Morocco. *Math. Model. Nat. Phenom.* **2020**, *15*, 31. [[CrossRef](#)]
21. Bouchnita, A.; Chekroun, A.; Jebrane, A. Mathematical Modeling Predicts That Strict Social Distancing Measures Would Be Needed to Shorten the Duration of Waves of COVID-19 Infections in Vietnam. *Front. Public Health* **2021**, *8*, 559693. [[CrossRef](#)]
22. Sorokowska, A.; Sorokowski, P.; Hilpert, P.; Cantarero, K.; Frackowiak, T.; Ahmadi, K.; Alghraibeh, A.M.; Aryeetey, R.; Bertoni, A.; Bettache, K.; et al. Preferred Interpersonal Distances: A Global Comparison. *J. Cross Cult. Psychol.* **2017**, *48*, 577–592. [[CrossRef](#)]
23. Nguyen, L.H.; Drew, D.A.; Graham, M.S.; Joshi, A.D.; Guo, C.G.; Ma, W.; Mehta, R.S.; Warner, E.T.; Sikavi, D.R.; Lo, C.-H.; et al. Risk of COVID-19 among front-line health-care workers and the general community: A prospective cohort study. *Lancet Public Health* **2020**, *5*, e475–e483. [[CrossRef](#)]
24. Klompas, M.; Baker, M.; Rhee, C.; Tucker, R.; Fiumara, K.; Griesbach, D.; Bennett-Rizzo, C.; Salmasian, H.; Wang, R.; Wheeler, N.; et al. A SARS-CoV-2 Cluster in an Acute Care Hospital. *Ann. Intern. Med.* **2021**, *174*, 794–802. [[CrossRef](#)]
25. Goldberg, L.; Levinsky, Y.; Marcus, N.; Hoffer, V.; Gafner, M.; Hadas, S.; Kraus, S.; Mor, M.; Scheuerman, O. SARS-CoV-2 Infection Among Health Care Workers Despite the Use of Surgical Masks and Physical Distancing—the Role of Airborne Transmission. *Open Forum Infect. Dis.* **2021**, *8*, ofab036. [[CrossRef](#)]
26. Wells, W.F. *Airborne Contagion and Air Hygiene. An Ecological Study of Droplet Infections*; Harvard University Press: Cambridge, MA, USA, 1955.
27. Riley, E.; Murphy, G.; Riley, R. Airborne spread of measles in a suburban elementary school. *Am. J. Epidemiol.* **1978**, *107*, 421–432. [[CrossRef](#)]
28. Riley, R.L. Airborne infection. *Am. J. Med.* **1974**, *57*, 466–475. [[CrossRef](#)]
29. Gammaitoni, L.; Nucci, M.C. Using a mathematical model to evaluate the efficacy of TB control measures. *Emerg. Infect. Dis.* **1997**, *3*, 335–342. [[CrossRef](#)]
30. Buonanno, G.; Stabile, L.; Morawska, L. Estimation of airborne viral emission: Quanta emission rate of SARS-CoV-2 for infection risk assessment. *Environ. Int.* **2020**, *141*, 105794. [[CrossRef](#)]
31. Dai, H.; Zhao, B. Association of infected probability of COVID-19 with ventilation rates in confined spaces. *Build. Simul.* **2020**, *13*, 1321–1327. [[CrossRef](#)]
32. Lau, Z.; Griffiths, I.M.; English, A.; Kaouri, K. Predicting the Spatially Varying Infection Risk in Indoor Spaces Using an Efficient Airborne Transmission Model. *Proc. R. Soc. A* **2022**, *478*, 20210383. [[CrossRef](#)]
33. Kaban, B.; Argoul, P.; Jebrane, A.; Cumunel, G.; Erlicher, S. A crowd movement model for pedestrian flow through bottlenecks. *Ann. Solid Struct. Mech.* **2016**, *8*, 1–15. [[CrossRef](#)]
34. Jebrane, A.; Argoul, P.; Hakim, A.; El Rhabi, M. Estimating contact forces and pressure in a dense crowd: Microscopic and macroscopic models. *Appl. Math. Model.* **2019**, *74*, 409–421. [[CrossRef](#)]
35. Wang, P. Understanding Social-Force Model in Psychological Principles of Collective Behavior. *arXiv* **2017**, arXiv:1605.05146v11.
36. Bosina, E.; Weidmann, U. Estimating pedestrian speed using aggregated literature data. *Phys. A Stat. Mech. Appl.* **2017**, *468*, 1–29. [[CrossRef](#)]

37. Willis, A.; Gjersoe, N.; Havard, C.; Kerridge, J.; Kukla, R. Human Movement Behaviour in Urban Spaces: Implications for the Design and Modelling of Effective Pedestrian Environments. *Environ. Plann. B Plann. Des.* **2004**, *31*, 805–828. [CrossRef]
38. Moussaïd, M.; Helbing, D.; Garnier, S.; Johansson, A.; Combe, M.; Theraulaz, G. Experimental study of the behavioural mechanisms underlying self-organization in human crowds. *Proc. R. Soc. B* **2009**, *276*, 2755–2762. [CrossRef]
39. Ma, J.; Song, W.G.; Fang, Z.M.; Lo, S.M.; Liao, G.X. Experimental study on microscopic moving characteristics of pedestrians in built corridor based on digital image processing. *Builde. Environ.* **2010**, *45*, 2160–2169. [CrossRef]
40. Seer, S.; Rudloff, C.; Matyus, T.; Brändle, N. Validating Social Force based Models with Comprehensive Real World Motion Data. *Transp. Res. Proc.* **2014**, *2*, 724–732. [CrossRef]
41. Bassoli, E.; Vincenzi, L. Parameter Calibration of a Social Force Model for the Crowd-Induced Vibrations of Footbridges. *Front. Built Environ.* **2021**, *7*, 75. [CrossRef]
42. Kretz, T.; Lohmiller, J.; Sukennik, P. Some Indications on How to Calibrate the Social Force Model of Pedestrian Dynamics. *Transp. Res. Rec.* **2018**, *2672*, 228–238. [CrossRef]
43. Taherifar, N.; Hamedmoghadam, H.; Sree, S.; Saberi, M. A macroscopic approach for calibration and validation of a modified social force model for bidirectional pedestrian streams. *Transp. A Transp. Sci.* **2018**, *15*, 1637–1661. [CrossRef]
44. Haut Commissariat du Plan. Available online: [https://www.hcp.ma/Les-Cahiers-du-Plan-N-43-Mars-Avril-2013\\_a1248.html](https://www.hcp.ma/Les-Cahiers-du-Plan-N-43-Mars-Avril-2013_a1248.html) (accessed on 15 November 2022).
45. Montero, P.; Loukid, M. Croissance des enfants de la ville de Marrakech (Maroc): Analyse comparative avec des enfants espagnols. *Bull. Mem. Soc. Anthropol. Paris* **1991**, *3*, 211–224. [CrossRef]
46. Mellouki, N. Vieillesse et Mode Alimentaire: étude Anthropologique à Marrakech. Ph.D. Thesis, Université Cadi Ayyad, Marrakesh, Morocco, 2007.
47. Ministère de la Santé. Available online: <https://www.sante.gov.ma/Documents/2019/05/Rapport%20de%20l%20enqu%C3%AAte%20Stepwise.pdf> (accessed on 15 November 2022).
48. Rastogi, R.; Thaniarasu, I.; Chandra, S. Design Implications of Walking Speed for Pedestrian Facilities. *J. Transp. Eng.* **2011**, *137*, 687–696. [CrossRef]
49. Shaw, G.; Williams, A.M. *Tourism and Tourism Spaces*; SAGE Publications: Thousand Oaks, CA, USA, 2004.
50. United Nations. Available online: <https://www.un.org/development/desa/pd/content/household-size-and-composition-around-world-2017-data-booklet> (accessed on 15 February 2022).
51. Trading Economics. Available online: <https://tradingeconomics.com/morocco/employment-rate> (accessed on 15 February 2022).
52. The World Bank. Available online: <https://data.worldbank.org/indicator/SE.SEC.ENRL.TC.ZS?locations=MA> (accessed on 1 March 2022).
53. Ministère de l'éducation Nationale. Available online: [https://www.men.gov.ma/Ar/Documents/Recueil2012-13\\_v25032013.pdf](https://www.men.gov.ma/Ar/Documents/Recueil2012-13_v25032013.pdf) (accessed on 5 December 2022).
54. World Health Organization. Available online: <http://www.who.int/news-room/questions-and-answers/item/coronavirus-disease-covid-19-how-is-it-transmitted> (accessed on 2 March 2022).
55. Tang, J.W.; Marr, L.C.; Li, Y.; Dancer, S.J. COVID-19 has redefined airborne transmission. *BMJ* **2021**, *373*. [CrossRef] [PubMed]
56. Tang, J.; Bahnfleth, W.; Bluysen, P.; Buonanno, G.; Jimenez, J.; Kurnitski, J.; Li, Y.; Miller, S.; Sekhar, C.; Morawska, L.; et al. Dismantling myths on the airborne transmission of severe acute respiratory syndrome coronavirus-2 (SARS-CoV-2). *J. Hosp. Infect.* **2021**, *110*, 89–96. [CrossRef] [PubMed]
57. Gorbunov, B. Aerosol Particles Generated by Coughing and Sneezing of a SARS-CoV-2 (COVID-19) Host Travel over 30 m Distance. *Aerosol. Air Qual. Res.* **2021**, *21*, 200468. [CrossRef]
58. To, K.K.W.; Tsang, O.T.Y.; Yip, C.C.Y.; Chan, K.H.; Wu, T.C.; Chan, J.M.C.; Leung, W.S.; Chik, T.S.H.; Choi, C.Y.C.; Kandamby, D.H.; et al. Consistent Detection of 2019 Novel Coronavirus in Saliva. *Clin. Infect. Dis.* **2020**, *71*, 841–843. [CrossRef] [PubMed]
59. Basu, S. Computational characterization of inhaled droplet transport in the upper airway leading to SARS-CoV-2 infection. *MedRxiv* **2020**. [CrossRef]
60. Riediker, M.; Tsai, D.H. Estimation of Viral Aerosol Emissions From Simulated Individuals with Asymptomatic to Moderate Coronavirus Disease 2019. *JAMA Netw. Open* **2020**, *3*, e2013807. [CrossRef]
61. Wang, Y.; Xu, G.; Huang, Y.W. Modeling the load of SARS-CoV-2 virus in human expelled particles during coughing and speaking. *PLoS ONE* **2020**, *15*, e0241539. [CrossRef]
62. van Doremalen, N.; Bushmaker, T.; Morris, D.H.; Holbrook, M.G.; Gamble, A.; Williamson, B.N.; Tamin, A.; Harcourt, J.L.; Thornburg, N.J.; Gerber, S.I.; et al. Aerosol and Surface Stability of SARS-CoV-2 as Compared with SARS-CoV-1. *N. Engl. J. Med.* **2020**, *382*, 1564–1567.
63. Hallett, S.; Toro, F.; Ashurst, J. *Physiology, Tidal Volume*; StatPearls: Treasure Island, FL, USA, 2022.
64. Sadria, M.; Layton, A.T. Modeling within-Host SARS-CoV-2 Infection Dynamics and Potential Treatments. *Viruses* **2021**, *13*, 1141. [CrossRef]
65. Noh, J.; Danuser, G. Estimation of the fraction of COVID-19 infected people in U.S. states and countries worldwide. *PLOS ONE* **2021**, *16*, e0246772. [CrossRef]
66. The World Health Organization. Available online: <https://covid19.who.int/region/emro/country/ma> (accessed on 1 December 2022).

67. Sankhyan, S.; Heinselman, K.N.; Ciesielski, P.N.; Barnes, T.; Himmel, M.E.; Teed, H.; Patel, S.; Vance, M.E. Filtration Performance of Layering Masks and Face Coverings and the Reusability of Cotton Masks after Repeated Washing and Drying. *Aerosol Air Qual. Res.* **2021**, *21*, 210117. [CrossRef]
68. Yang, X.; Wang, Q. Crowd Hybrid Model for Pedestrian Dynamic Prediction in a Corridor. *IEEE Access* **2019**, *7*, 95264–95273. [CrossRef]
69. Campanella, M.; Hoogendoorn, S.P.; Daamen, W. Effects of Heterogeneity on Self-Organized Pedestrian Flows. *Transp. Res. Rec.* **2009**, *2124*, 148–156.
70. Centre for Disease Control and Prevention. Available online: <https://www.cdc.gov/coronavirus/2019-ncov/prevent-getting-sick/prevention.html> (accessed on 15 March 2022).
71. Moroccan Ministry of Health. Available online: [https://www.sante.gov.ma/Publications/Pages/Bullten\\_épidémiologique.aspx](https://www.sante.gov.ma/Publications/Pages/Bullten_épidémiologique.aspx) (accessed on 3 June 2022).
72. Magdy Beshbishy, A.; Hetta, H.F.; Hussein, D.E.; Saati, A.A.; Uba, C.C.; Rivero-Perez, N.; Zaragoza-Bastida, A.; Shah, M.A.; Behl, T.; Batiha, G.E.S. Factors associated with increased morbidity and mortality of obese and overweight COVID-19 patients. *Biology* **2020**, *9*, 280. [CrossRef]
73. Malik, V.S.; Ravindra, K.; Attri, S.V.; Bhadada, S.K.; Singh, M. Higher body mass index is an important risk factor in COVID-19 patients: A systematic review and meta-analysis. *Environ. Sci. Pollut. Res.* **2020**, *27*, 42115–42123. [CrossRef]
74. Goyal, A.; Reeves, D.B.; Cardozo-Ojeda, E.F.; Schiffer, J.T.; Mayer, B.T. Viral load and contact heterogeneity predict SARS-CoV-2 transmission and super-spreading events. *Elife* **2021**, *10*, e63537. [CrossRef]
75. Tcharkhtchi, A.; Abbasnezhad, N.; Zarbini Seydani, M.; Zirak, N.; Farzaneh, S.; Shirinbayan, M. An overview of filtration efficiency through the masks: Mechanisms of the aerosols penetration. *Bioact. Mater.* **2021**, *6*, 106–122. [CrossRef]
76. Ou, C.; Hu, S.; Luo, K.; Yang, H.; Hang, J.; Cheng, P.; Hai, Z.; Xiao, S.; Qian, H.; Xiao, S.; et al. Insufficient ventilation led to a probable long-range airborne transmission of SARS-CoV-2 on two buses. *Build. Environ.* **2022**, *207*, 108414. [CrossRef]
77. Moreno, J.C.; Puzzo, M.L.R.; Paul, W. Collective dynamics of pedestrians in a corridor: An approach combining social force and Vicsek models. *Phys. Rev. E* **2020**, *102*, 022307. [CrossRef]
78. Pecol, P.; Argoul, P.; Dal Pont, S.; Erlicher, S. A new crowd movement modeling for pedestrians who hold hands. In Proceedings of the XVIIIth Symposium Vibrations, Chocs et Bruit & ASTELAB, Clamart, France, 3–7 July 2012; EDF: Clamart, France, 2012; 9p.
79. Hanna, S.R.; Briggs, G.A.; Hosker, R.P., Jr. *Handbook on Atmospheric Diffusion*; National Oceanic and Atmospheric Administration: Oak Ridge, TN, USA, 1982; p. 103. [CrossRef]

**Disclaimer/Publisher’s Note:** The statements, opinions and data contained in all publications are solely those of the individual author(s) and contributor(s) and not of MDPI and/or the editor(s). MDPI and/or the editor(s) disclaim responsibility for any injury to people or property resulting from any ideas, methods, instructions or products referred to in the content.